The effect of solution annealing on additively manufactured and hot isostatically pressed René 80 Ni-based superalloy

Journal of Materials Research and Technology 33 (2024) 6591–6600

Contents lists available at ScienceDirect

Journal of Materials Research and Technology

journal homepage: www.elsevier.com/locate/jmrt

The effect of solution annealing on additively manufactured and hot isostatically pressed René 80 Ni-based superalloy

M.S. Kenevisi [a,b,*], P.A. Martelli [a,b], I. Titonel [a], E. Bassini [a,c], G. Marchese [a,b], D. Ugues [a,c]

[a] Department of Applied Science and Technology (DISAT), Politecnico di Torino, Italy
[b] Integrated Additive Manufacturing IAM@PoliTO Center, Politecnico di Torino, Italy
[c] National Interuniversity Consortium of Materials Science and Technology (INSTM), Italy

ARTICLE INFO

Handling editor: L Murr

Keywords:
Nickel superalloy
René 80
Additive manufacturing
Precipitation
Microstructure

ABSTRACT

The effect of solution annealing temperature on the microstructure, morphology, size, and volume fraction of γ′ precipitates, and hardness of the material was investigated in this work. Samples were fabricated by Laser Based Powder Bed Fusion (LB-PBF) process and post processed with Hot isostatically Pressing (HIP). Next, different solution annealing conditions were applied to assess their impact on γ′ precipitation. The microstructure of the samples was characterized by light optical microscopy (LOM), field emission scanning electron microscopy (FE-SEM), and electron backscattered diffraction (EBSD). Defects were assessed by treating LOM images through ImageJ. The hardness was also measured by Brinell hardness. The results showed that HIP process densified the samples and increased the relative density to more than 99.98%. Performing HIP and solution annealing at a sub-solvus temperature resulted in irregular-shaped γ′ precipitates and grains remained elongated along the building direction. By increasing the solutioning temperature above solvus treatment, organized and cubic precipitates formed. Moreover, by increasing the solutioning temperature from 1230 to 1270 °C the grain size increased from 15 to 46 μm, and consequently, the hardness decreased by about 6%. The results also revealed that the γ′ volume fraction was not greatly affected by the solutioning temperature and remained within the range of 20.4–22.3% after aging. Finally, a thermal setpoint of 1260 °C resulted the most promising condition for solution annealing PBF-LB René 80 superalloy to obtain cubic secondary γ′ precipitates, minimizing the presence of irregular γ' at grain boundaries and providing a robust process against thermal oscillations within industrial furnaces.

1. Introduction

René 80 is a precipitation hardening Nickel-based superalloy typically used in the aeronautical and energy production fields, where the in-service conditions demand high thermo-mechanical properties and resistance to corrosion [1,2]. In particular, the alloy is designed to stand working temperature above 800 °C [3]. The thermo-mechanical properties are mainly given by the precipitation of the ordered $L1_2$ γ′ phase, which has stoichiometry Ni_3(Al, Ti) [4]. The volume fraction, size and shape of the γ′ particles determine the effectiveness of the reinforcement [5–8]. For example, an increase in the volume fraction of the precipitates has proven positive effects on the thermo-mechanical properties of these superalloys [6,8]. Alongside the volume fraction, the mechanical properties of the superalloys are affected by the shape of the γ′ due to its correlation with the lattice misfit between the matrix γ and γ' [9]; indeed, round particles are associated to lattice misfits up to 0.2%, while cubic γ' is associated to lattice misfits between 0.5 and 1% [10,11].

For precipitation hardening superalloy like René 80, post-process heat treatments play a crucial role to properly design the final microstructure and its effectiveness in terms of thermo-mechanical properties. These superalloys are subjected to a multiple step heat treatment consisting of solution annealing and, usually, a double ageing step [10,12]. The solution annealing is performed above the γ′ solvus temperature to dissolve the coarse and irregular primary γ′ formed during the investment casting, which represents the traditional manufacturing route for this superalloy. First aging is then applied below the γ′ solvus to let the γ′ nuclei grow up to dimensions of few hundreds of nanometers. Finally, second aging is performed at a lower temperature to reach the hardness peak of the alloy and stabilize the microstructure. In strategic sectors like aeronautics, alternative additive manufacturing routes are nowadays explored. In so demanding sectors both for investment cast and

* Corresponding author. Department of Applied Science and Technology (DISAT), Politecnico di Torino, Italy.
E-mail address: saleh.kenevisi@polito.it (M.S. Kenevisi).

https://doi.org/10.1016/j.jmrt.2024.11.003
Received 8 August 2024; Received in revised form 1 November 2024; Accepted 1 November 2024
Available online 2 November 2024

Table 1
– Chemical composition (wt.%) of the René 80 powder used in the study.

Element	Cr	Co	Mo	Al	Ti	W	Hf	Ni
wt.%	14.0	9.0	4.0	3.0	4.7	4.0	0.8	bal.

additively manufactured parts, an additional Hot Isostatic Pressing (HIP) step is usually applied before the heat treatment below the γ′ solvus. The main goal of this latter production stage is to close possible residual defects inherited from the manufacturing process and reach the maximum densification [13]. This aspect becomes particularly important when dealing with additive manufacturing technologies, like the Laser Based Powder Bed Fusion (PBF-LB). The latter has gained important attention from the scientific and industrial community to process Nickel-based superalloys, mainly due to its flexibility and freedom of design [14,15]. However, the high content of γ′ forming elements like Al and Ti makes some of these superalloys difficult-to-weld and thus challenging to process by PBF-LB due to the formation of a pronounced fraction of residual defects [16–18]. The authors have previously demonstrated the possibility to properly process René 80 with PBF-LB, minimizing the residual defects through parameters optimization, but residual densification flaws inherited from the PBF-LB are still present, making the use of HIP practically mandatory [14]. Moreover, the rapid heating-cooling cycles results into microstructural features which are different form the typical ones obtained by investment casting. Actually, PBF-LB microstructures show very thin and textured grains elongated along the building directions, and the matrix remains oversaturated with no detectable signs of γ′ precipitation [14,19,20]. For these reasons, the deepening and optimization of post-processing of Nickel-based superalloys is currently deeply studied in the literature [19,21–23]. However, despite its strategic importance, no works regarding the study of heat treatments of PBF-LB René 80 can be found in the literature so far up to the authors' knowledge. The effect of the heat treatments on the microstructure of René 80 has been studied only in the cast state [1,24,25].

In the present work, the effects of HIP and heat treatments have been studied on René 80 superalloy processed with PBF-LB using a previously developed parameters' set [14]. In particular, the study focuses on the optimization of the solution annealing step, which is critical in determining the final size and shape of the γ′ particles [19]. Different solution annealing temperatures (from 1230 °C to 1270 °C) have been applied to PBF-LB René 80 specimens alongside subsequent first aging to measure the resulting microstructure in terms of γ′ fraction, shape and size, hardness and grain recovery and growth. The results showed that it is possible to obtain cubic γ' precipitates and recovery and growth of the initial thin and elongated grains after first aging, when the solution annealing setpoint is imposed at 1260 °C. The sub-solvus HIP was also applied to as-built samples, enabling to overcome the 99.98% of densification. These results represent an important milestone in defining the optimal heat-treatment recipes to process difficult-to-weld Nickel based superalloy René 80 through PBF-LB process.

2. Experimental procedure

2.1. Material and process

This study used René 80 gas-atomized powder (NI 183-4) supplied by Praxair Co. The nominal chemical composition of the powder is given in Table 1. The nominal range for the size of the powder particles was 16–45 μm with D10 = 17.9 μm, D50 = 28.9 μm, and D90 = 43.7 μm, as determined by laser granulometry.

Powder morphology was characterized by scanning electron microscopy (SEM); the results are shown in Fig. 1a and b.

Some cold splats and satellites can be seen attached to the particles. However, as they are limited, the powder-spreadability is unaffected. Additionally, it was observed that the particles have a cellular and dendritic structure due to the atomization process's high cooling rate. The high cooling rates do not allow enough time for solute redistribution within the solidifying droplets, leading to a non-equilibrium solidification process. This results in microstructures such as dendrites or cellular structures, which is affected by the temperature gradient (G) and the solidification rate (R) [26,27].

Cubic samples of 20 × 20 × 20 mm^3 were fabricated by PBF-LB process using a Printsharp 250 machine on a low-alloyed carbon steel platform. Additionally, a sample with a height of 30 mm was produced to perform defect analysis in the as-built condition. A bi-directional scanning strategy was used in this work, where the scanning direction was rotated by 67° for each successive layer. The process parameters have been optimized elsewhere by the authors and replicated for this work [14].

2.2. Post-processing heat treatment

Hot Isostatic Pressing (HIP) followed by different solution heat treatments were applied, and the resulting microstructure was assessed in depth. A further reduction of defects within the PBF-LB as-built samples was achieved using a HIP furnace model QIH15L produced by Quintus Technologies AB. The process was undertaken in a sub-solvus regime using times, pressure and temperatures compatible with the Nickel-based alloys families. Due to confidentiality reasons, actual values cannot be disclosed. Solution annealing and first aging processes were carried out in a TAV Minijet low-pressure furnace with an operating pressure of 10^{-3} mbar. Nitrogen gas at 1.5 bar was used as quenching media. The heating rate and the soaking time during the solution annealing were kept constant at 10 °C/min and 2 h respectively. The samples were cooled to 900 °C with a constant cooling rate within the range from 50 to 70 °C/min and then heated to the aging temperature. More specifically, this latter part of the treatment was performed at 1095 °C for 4 h and followed by gas quenched with identical parameters as before down to room temperature. For the sake of easiness, solutioned and aged samples are labelled Sol12XX depending on the setpoint temperature of the treatment. All the experimental plans can be summarized in Table 2.

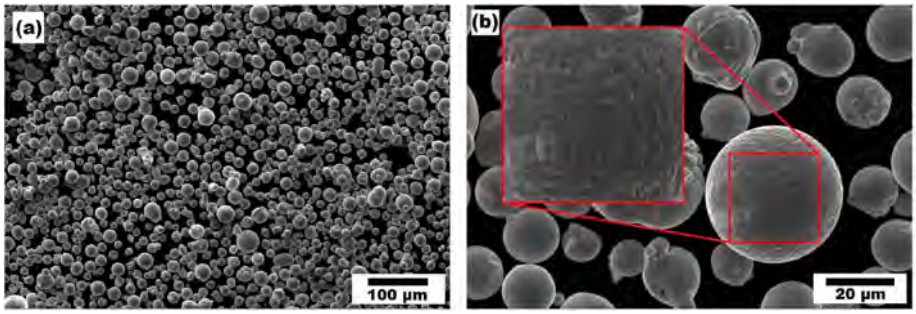

Fig. 1. – SEM micrographs of powder particles at different magnifications: a) 300× and b) 2000X.

Table 2
– Details of different heat treatments performed on the samples.

Sample code	Heat treatment
HIPtrad	HIP treatment performed at a sub-solvus temperature
Sol1230	HIP trad + solution annealing at 1230 °C/2h + aging at 1095/4h
Sol1245	HIP trad + solution annealing at 1245 °C/2h + aging at 1095/4h
Sol1260	HIP trad + solution annealing at 1260 °C/2h + aging at 1095/4h
Sol1270	HIP trad + solution annealing at 1270 °C/2h + aging at 1095/4h

2.3. Sample preparation

Concerning the microstructural characterization, the specimens were cut along and perpendicularly to the building direction, i.e., along XZ and XY planes. The specimens were then mounted in epoxy resin and ground using SiC papers up to 1200 grit, then polished by 6, 3, and 1 μm diamond suspensions. At the last polishing step, 0.04 μm colloidal silica was used to obtain a mirror-like surface for the microstructural evaluations. The specimens were electrolytically etched with 30% H_3PO_4 water solution, applying a voltage of 3.5V for ca. 5 s to reveal γ' morphology and its gradual structural changes. Additionally, where the quantification of the γ' phase was required, the specimens were etched by Kalling's No.2 solution.

2.4. Defect analysis

Flaws' population was analyzed in the "As built", "HIPtrad", and "HIPtrad + Sol1260″ conditions to assess the healing effect of the HIP. In particular, a metallographic section parallel to the building direction was cut, and 15 images of approximately 2.63 mm^2 each per surface were acquired using a Leica DZ500 light optical microscope (LOM). The acquired images were then processed using ImageJ software. An algorithm developed by the authors was used for flaws segmentation, and the flowchart is reported in Fig. 2.

In the as-built condition, flaws were also divided into three different categories: (i) gas porosities, (ii) lack of fusion and (iii) cracks. The authors discussed the nature of these flaws in René 80 alloy in a previous work [28]. This segmentation rule was not considered for the samples after HIP, because after the healing process, defects were too small and geometrically similar one to each other and it was too difficult to distinguish. More specifically, only small round pores could be observed after HIP, making the abovementioned separation of little help.

2.5. Microstructural characterization

A Leica Z500 light-optical microscope (LOM) was used to assess the grain size in both XZ and XY planes. The average grain size was

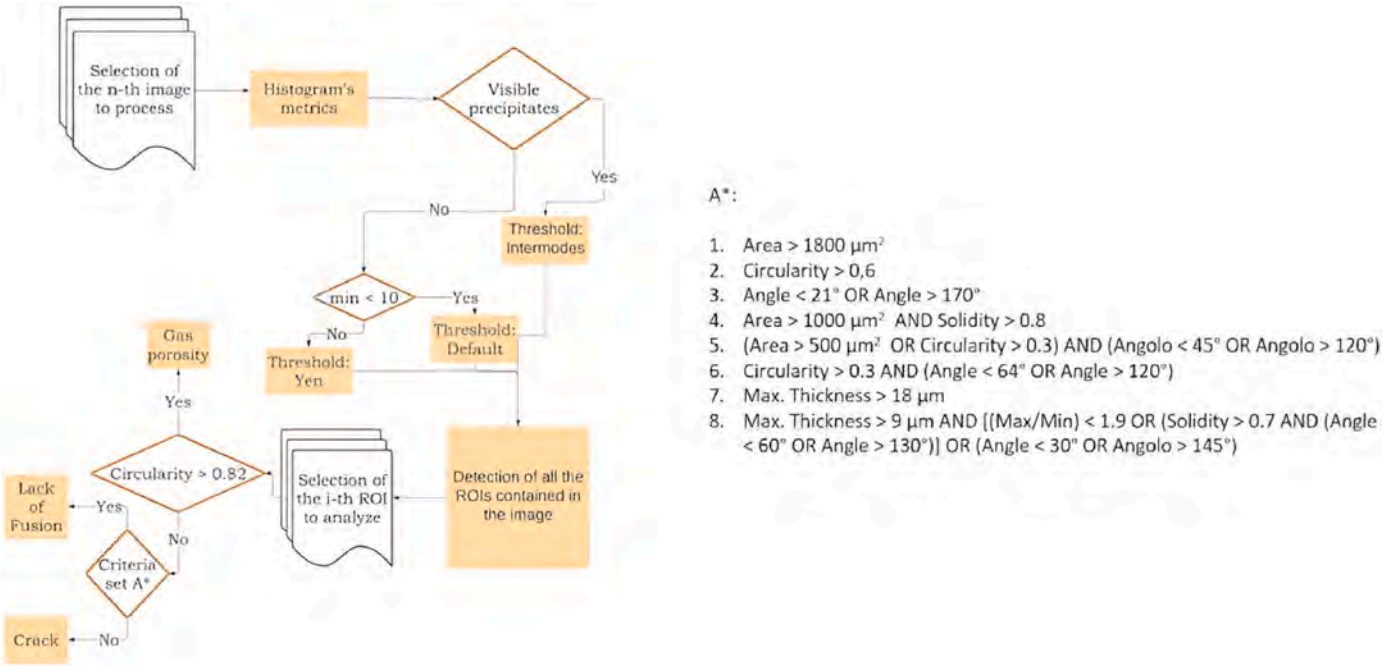

Fig. 2. Flowchart for the segmentation of densification flaws in ImageJ.

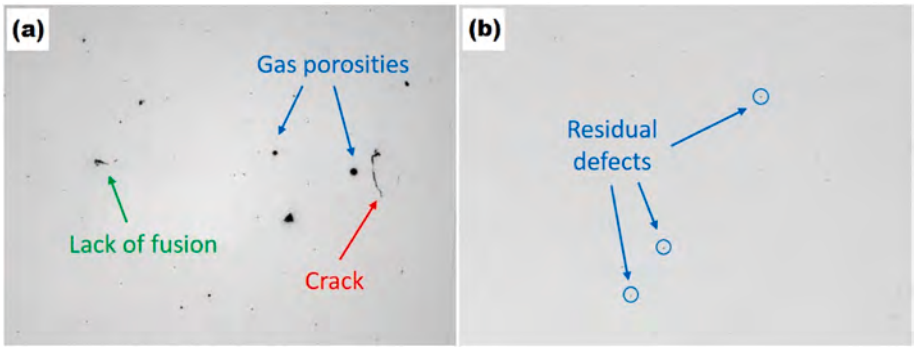

Fig. 3. Images taken at 100x under LOM a) in as-built condition and b) after HIP.

Table 3
Defects measured in the as-built condition. The results were obtained by analyzing 15 images at 50x under LOM in XZ section.

	Gas porosities	Lack of fusion	Cracks density
As-built	0.018 ± 0.012 %	0.048 ± 0.036 %	0.044 ± 0.005 mm/mm^2

Table 4
Total defects fraction measured in the as-built sample and after HIP. The results were obtained analyzing 15 images at 50x under LOM in XZ section.

	As-built	HIP
Total defects fraction	0.078 ± 0.041 %	0.016 + 0.006/- %

measured using the intercept method [29]. A Zeiss Merlin field emission scanning electron microscope (FE-SEM) equipped with a Gemini III column and a Tescan S9000G focused ion beam scanning electron microscope (FIB-SEM) equipped with Oxford symmetry electron backscattered diffraction (EBSD) detector were used to study the material microstructure focusing on γ′ size, fraction and distribution. ImageJ software was used to assess the average fraction area and the average size of γ′ particles by image analysis technique.

2.6. Hardness measurement

The hardness test was performed using an Emcotest M4U 025 Brinell hardness tester and applying 62.5 kg force for 15 s with a tungsten carbide indenter having a diameter of 2.5 mm. More specifically, three indentations in each sample orientation (XZ and XY) were performed for each sample to create a reliable statistical sampling.

3. Results and discussion

3.1. Defect assessment

The densification flaws from the PBF-LB process were analyzed before and after HIP using LOM to assess the effect of post processing. Fig. 3a shows the typical densification flaws inherited from the PBF-LB process in the as-built sample: gas porosities, lack of fusion and cracks. Conversely, Fig. 3b shows the XZ surface of the HIPed sample: just a few and very small residual defects can be detected at 100× magnifications.

The quantification results for one as-built sample are reported in Table 3. The results obtained for the as-built sample align with previous authors' findings [14]. Concerning the previous findings, the segmentation algorithm was developed to divide gas porosities and lack of fusion based on their morphology. The volume fraction of the former is much lower than the fraction of lacks of fusion. Indeed, lacks of fusion are typically larger than gas porosities and result in a higher fraction.

The HIPed sample was also analyzed to assess HIP's capability to recover the densification flaws. However, during the HIP step, the defects collapse. The segmentation parameters are no longer suitable to distinguish among all the previously discussed defects, which now uniformly appear as spherical pores. Consequently, after the HIP, the flaws population could be analyzed only in terms of generic defects. To provide a correct comparison, the total fraction for all types of defects was calculated for the as-built and the HIP state, and the results are reported in Table 4 for comparison. The densification of the PBF-LB René 80 overcomes the 99.98 % after HIP, and this result testifies the importance of HIP for difficult-to-process Nickel superalloys.

3.2. Microstructural evolution

Fig. 4 shows the microstructure of the as-built sample in the XY and the XZ planes.

Melt pools are clearly visible in the section across the building direction. It is characterized by varying sizes due to the rotation of the printing direction at each layer. However, it can be observed that, within each layer, the melt pools maintain similar dimensions, as can also be seen in other Ni-based alloys shown by Marchese et al. [30]. The scanning strategy's effect on the grains' orientations can be seen in Fig. 4a. As illustrated, the passes have a misorientation angle of about 67°. Additionally, the microstructure shows elongated grains along the building direction and a columnar dendritic structure resulting from the manufacturing process that involves a high cooling rate, which is in the order of 10^5–10^7 °C/s [31]. Therefore, this combination of high thermal gradients and rapid cooling rates resulted in the columnar dendritic structure, which is a typical feature of parts manufactured by PBF-LB.

It is known that a microstructure consisting of equiaxed grains and uniformly distributed γ′ precipitates would have improved mechanical properties even at high temperatures compared to those of an as-built one. To achieve this transformation, a thermal post process is required. As the γ′ precipitation process is based on the nucleation and growth process, heat treatment can significantly affect the shape, volume fraction, structure, and size of the precipitates [32,33]. Generally, in Ni-based superalloys, a microstructure consisting of ordered cuboidal γ′ precipitates is favorable as discussed in the introduction. Therefore, different heat treatments were applied to improve the microstructural characteristics in terms of γ′ precipitation, aiming at maximizing their volume fraction and achieving an ordered cuboidal structure. More specifically, to separate the effects of HIP alone from the results of the complete heat treatment, this initial step was assessed as a separate case study.

Firstly, the as-built samples were HIPped, and after the required soaking time, simple natural cooling was applied within the furnace. In other words, samples were cooled within the HIP furnace only through the heat exchange between the samples and the water-cooled walls of the equipment, as happens typically in traditional HIP facilities. Fig. 5 depicts the general microstructure of the HIPed sample. Fig. 5a and b shows the grains observed with LOM. It can be observed that, while the meltpools are no longer visible, the microstructure is still characterized by thin grains elongated in the building direction. Fig. 5c shows that fan-like γ' particles form within the grains, while larger and highly

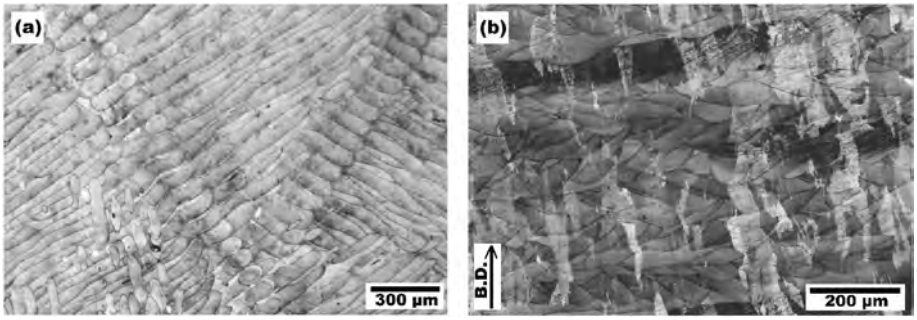

Fig. 4. – Micrographs of the sample in as-built condition along a) XY and b) XZ planes.

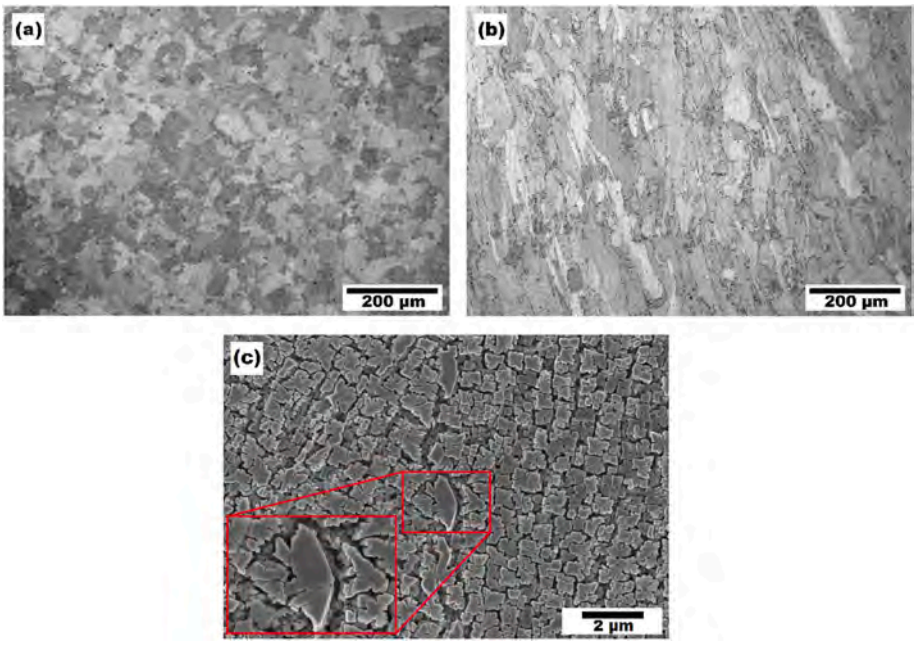

Fig. 5. – Cross-sections of the HIPtrad sample in the a) XY and b,c) XZ plane.

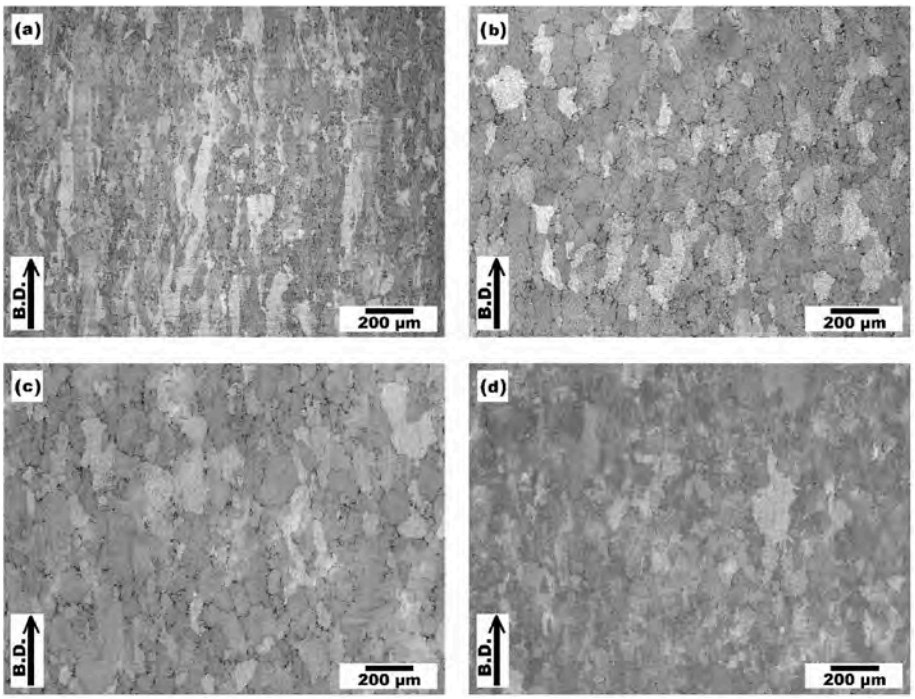

Fig. 6. – Microstructure of the samples along the building direction and solution annealed at: a) 1230 °C, b) 1245 °C, c) 1260 °C, and d) 1270 °C.

irregularly shaped ones at the grain boundaries.

The sub-solvus HIP does not provide sufficient energy to trigger the recrystallization process, and the grains remain thin and elongated. Moreover, primary γ' at the grain boundaries remains undissolved, hindering the grain boundary growth during the treatment.

Quantitative analysis was also performed. The grain size resulted in 45.5 ± 8.6 μm and 22 ± 0.7 μm in the XZ and XY planes, respectively, with a calculated aspect ratio of 2.0.

In HIPtrad condition, large particles of irregular-shaped γ' in a size of up to 1 μm and a fan-type γ-γ' structure can be seen in the microstructure (Fig. 5c), which is related to the slow cooling rate of the process [34]. Supersaturation, relatively higher diffusivity between the matrix and precipitates at low cooling rates, and low nucleation density are some factors responsible for the irregular growth of the precipitates [35]. It should be noted that since the sample is HIPed at a sub-solvus temperature, the formation of γ' derives from the solid-state diffusion of Al and Ti from the over saturated matrix obtained at the printing stage. It is also reported that the elongated γ' blocks tend to form on the grain boundaries while the fan-type precipitates nucleate within the grains [24]. Generally speaking, the obtained γ' particles have different sizes and are irregularly shaped, suggesting that HIP treatment could not be the sole process to optimize the material microstructure. Analyzing the

Table 5
– Equivalent size of the grains (μm) in different conditions measured in the XZ and XY planes.

Condition	Sol1230, XY	Sol1230, XZ	Sol1245, XY	Sol1245, XZ	Sol1260, XY	Sol1260, XZ	Sol1270, XY	Sol1270, XZ
$\bar{d}$ (μm)	15 ± 4.6	45 ± 0.4	29 ± 18.3	44 ± 3.2	46 ± 9.8	58 ± 1.8	59 ± 3.1	75 ± 7.5

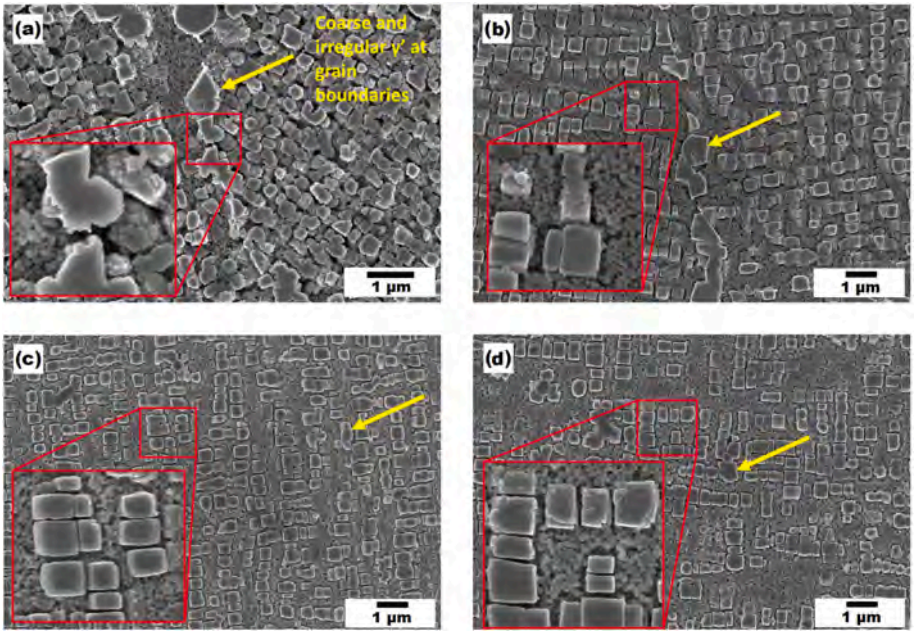

Fig. 7. – FE-SEM micrographs revealing the morphology of the precipitates at different conditions: a) Sol1230, b) Sol1245, c) Sol1260, and d) Sol1270. Yellow arrows indicate irregular primary γ′ particles at grain boundaries.

micrographs by ImageJ revealed that the volume fraction of γ′ is about 20–25%, which is comparable to those of solution-annealed samples. However, by lowering the cooling rate, the area fraction of γ′ precipitates tends to slightly increase due to the suitable condition for growth of γ′ provided by lower cooling rates [36].

After observing the result obtained with the HIP treatment, i.e. insufficient microstructure rearrangement, different heat treatment procedures were applied to optimize the solution annealing step. Samples were solution annealed at 4 different temperatures (1230, 1245, 1260, and 1270 °C) for 2 h. Fig. 6 illustrates the micrographs of the cross-sections in the XZ plane.

The morphology of the grains is significantly affected by the solution annealing temperature. Fig. 6a shows that after solution annealing at 1230 °C the grain structure is comparable to what observed after subsolvus HIP (Fig. 5b). A larger number of equiaxed grains is observed when the solution annealing is raised at 1245 °C and above, suggesting the triggering of recrystallization and grain growth. The quantitative numerical data are provided in Table 5.

It should be noted that all examined conditions still show a certain degree of retained anisotropy when the grain size is measured in the XZ and XY planes, which suggests that René 80 processed with PBF-LB has a very low tendency to recrystallize, even at such high temperatures. Additionally, a limited grain coarsening along the building direction was seen at lower test temperatures (Sol1230 and Sol1245).

The calculation of the aspect ratio of the grains in the XZ plane revealed that the sample that is heat treated at 1230 °C has pronounced elongated grains, exhibiting an aspect ratio of 3.0, confirming that elongated grains remained in the microstructure. Thermal energy was insufficient to promote both γ’ dissolution and recrystallization.

Based on the results in Table 5, the grain size grows by raising the solution annealing temperature, which can be justified considering the higher thermal energy given to the system and the more intense dissolution of γ′ particles at the grain boundaries hence lowering their pinning effect. Even at higher temperatures, such as 1245 °C, grain size standard deviation is still considerably high. This result can be explained by considering two main factors: the limited number of grains measured with the intercept method, and secondly, PBF-LB materials can be characterized by a complex mix of smaller and larger grains close to each other, whose growth can be irregularly distributed during heat treatments. In this situation, there would be some locations where the grains are recrystallized and equiaxed and others where the microstructure still consists of elongated grains along the building direction. Grains tended to be more equiaxed, increasing the temperature, and by solutioning at 1245 °C and 1260 °C, the aspect ratio values decreased to 1.5 and 1.3, respectively. After the assessment of the grain size and morphology, γ′ precipitates were studied at higher magnifications to investigate the effect of solutioning temperature on the γ′ precipitation, and the micrographs are presented in Fig. 7, where yellow arrows highlight irregular primary γ’ particles at grain boundaries.

As shown in Fig. 7a, for the Sol1230 sample, γ′ is mainly formed as irregular-shaped precipitates, and a few cubic-shaped particles can be observed. Grain boundaries are fully decorated by coarse and irregular primary γ′ particles, as also observed in another Ni-based superalloy [37]. This is due to the increased diffusion rates of γ′-forming elements in these regions. These particles grow into adjacent grains that have different crystallographic orientations, coupled with the varying mobility. By increasing the solution annealing temperature to 1245 °C, γ′ precipitates tended to form more uniformly in the microstructure and as cubic particles as well (Fig. 7b). This suggests that the solvus temperature of the γ′ should be around this temperature. Nonetheless, γ′ with different morphologies was observed in the microstructure at different locations. Specifically, the phase was irregularly shaped close to grain boundaries, where primary γ′ remains visible. After the heat treatment, the primary and undissolved particles have smooth edges, while the

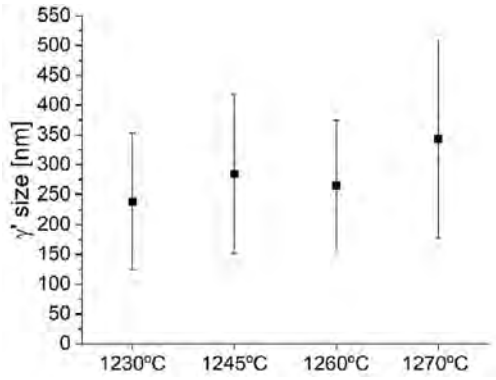

Fig. 8. The change in the size of γ′ particles as a function of solubilizing temperature estimated by three different methods.

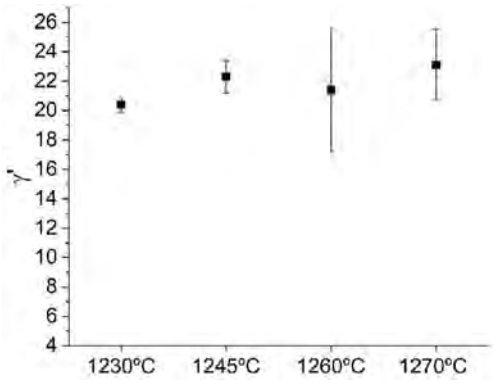

Fig. 9. γ′ fraction as a function of the solution annealing temperature.

secondary particles, which are dissolved and re-precipitated upon cooling, are regularly cuboidal and formed within the grains. Therefore, it can be concluded that the solution annealing temperature should be located slightly higher than 1245 °C.

Solutioning at higher temperatures (i.e. from 1260 °C, Fig. 7c) resulted in a homogeneous distribution of aligned and fully cubic γ′ precipitates. As reported by Johnson and Voorhees [38], the elastic interaction energy is the affecting parameter for the alignment of the precipitates. The cubic shape of the particles is related to the lattice misfit and, consequently, free energy. A coherent elastic stress can be produced around the precipitates by having a lattice misfit. As a result, the dominant part of the total free energy of the system would be the free energy that is induced by the aforementioned stress, which provides the favorable condition for precipitates to be cubic-shaped [39]. Additionally, increasing the solution annealing temperature makes the grain boundaries less detectable (due to progressive solutioning of primary gamma prime) and the matrix channels wider. Some primary γ' particles remain in the microstructure even after solution annealing at such temperatures, but they are smaller and fewer than after solution annealing at 1230 °C and 1245 °C. Nevertheless, it is worth mentioning that numerous very small tertiary γ′ precipitates were also detected within channels of γ matrix in the microstructure of solution annealed samples. These precipitates commonly form during cooling in the later stages of the heat treatment [40]. Generally, these precipitates can be seen after the second aging process. However, since the kinetic of γ′ precipitation is very fast, nuclei of spherical particles can be formed even during cooling from this early stage, leading to a bimodal distribution of secondary and tertiary precipitates. However, the highest fraction of these precipitates will be obtained only after the heat treatment completion.

According to the above discussion 1260 °C would be seen as an effective target temperature for solution annealing. The reason for investigating temperatures as high as 1270 °C is principally linked to industrial reasons since the furnace used during routine heat treatments may suffer a certain degree of uncertainty, typically ranging into a ±10 °C interval. Consequently, it is worth characterizing the microstructure within this temperature variation range with respect to the target temperature, to check whether any detrimental effects might occur. Assuming that the microstructure when solution annealing at 1250 °C would be very similar to that revealed at 1245 °C, we have explored only the upper boundary of the ±10 °C range around the set temperature. Comparing the microstructures, it can be seen that solution annealing at 1270 °C (Fig. 7d) did not result in incipient melting, which can lead to cracks. As discussed below, the amount of solubilized γ′ remained almost unchanged compared to the samples heat treated at temperatures close to the solvus temperature, i.e., 1260 °C. Moreover, no thermally induced porosity (TIP) was observed (according to Fig. 6d). However, by solutioning at a relatively high temperature (1270 °C), more irregular-shaped particles could be observed, which were also reported for other Ni-based superalloys [41]. Therefore, based on the results, it can be concluded that 1260 °C can be identified as an optimal solution annealing temperature, considering the thermal variability of the industrial furnaces. In this case, and considering the ±10 °C tolerance, the results showed that both 1250 °C and 1270 °C do not generate dramatic changes to the major optimized microstructural features of the material. Solution annealing well above the solvus temperature was not investigated within this work, since such treatments can result in incipient melting, TIPs, irregular-shaped precipitates, and a coarse-grain microstructure with deprived yield and ultimate tensile strengths due to the dissolution of grain boundary precipitates [42].

The quantitative results in terms of γ' size are reported in Fig. 8.

The measured mean Feret diameter is 239 ± 114 nm, 294 ± 133 nm, 265 ± 109 nm and 343 ± 166 nm after solution annealing at 1230 °C, 1245 °C, 1260 °C and 1270 °C, respectively. Considering the standard deviations, the size of the γ′ particles is not significantly affected by the solution annealing temperature, except for a slight coarsening after solution annealing at 1270 °C. This coarsening of the particles is related to the reduced interfacial energy and coherent strain energy of the matrix/precipitate interface at high temperatures [36]. However, the mean values of the measured diameters fall within the error bars' limits for all the solution annealing temperature. For this reason, it is unlikely that significant effects on the thermo-mechanical properties of the René 80 could take place.

The volume fraction of γ′ as a function of the solution annealing temperature is reported in Fig. 9.

The measured volume fraction of γ′ was 20.4 ± 0.5 %, 22.3 ± 1.1 %, 21.4 ± 4.2 %, 23.1 ± 2.4 %. The results showed that the solubilization temperature did not have a significant effect on the γ′ volume fraction, also considering the standard deviations. Generally, it is expected to have a lower volume fraction of precipitates for the solution-annealed sample at higher temperatures. In the present case the volume fraction was almost identical, with only a lower value at 1230 °C. It is worth mentioning that higher volume fractions are expected to be achieved after a subsequent second aging treatment, which is typical for these precipitation-hardening alloys. To wrap up the above-mentioned results, the solution annealing + first aging treatment does not significantly affect γ′ particles' size and volume fraction varying the solution annealing temperature, while the latter has a strong influence on the shape of precipitates. In other words, two different regions can be defined based on the solutioning temperature. When the temperature is lower than the critical temperature (in HIPtrad and Sol1230 samples), the microstructure consists of irregular-shaped γ′ precipitates. However, for temperatures higher than 1230 °C (in Sol1245, Sol1260, and Sol1270 samples), regular-shaped γ′ is dominant in the microstructure. The observations justify the importance in performing the solution annealing at sufficiently high temperature, above the threshold point at which the precipitates appear cuboidal in the first aged state; indeed, it

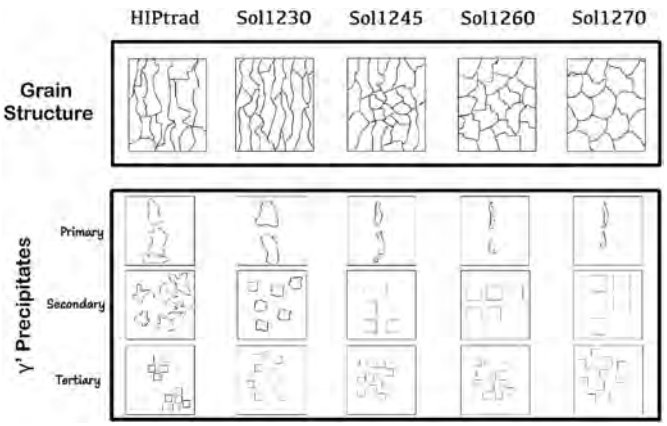

Fig. 10. – Schematic design of the effect of HIP and solution annealing temperature on the microstructure of the material.

is important to note that it is unlikely to obtain cubic γ' structure without applying the first aging process [19].

Fig. 10 schematically illustrates how different procedures (HIP and solution annealing at different temperatures) may affect the grain structure of the material and morphology of γ' precipitates.

Microstructure was, then, further investigated using EBSD technique, which is widely used to analyze the grain boundary misorientation distribution and any changes in the grain structure. Therefore, the grain recrystallization process was studied by EBSD technique. Samples with different conditions (as-built, HIPtrad, and heat-treated) were characterized and the crystal orientation maps are illustrated in Fig. 11.

It can be seen that in the as-built and HIPtrad conditions, the microstructure exhibits elongated grains along the building direction. Additionally, the annealed sample at a sub-solvus temperature (Sol1230) shows a microstructure remarkably similar to that observed after HIPping. The grains are still preferentially aligned along the building direction and with a high aspect ratio. This fact proves that even if the material is re-heated, microstructural evolution is limited unless the recrystallization threshold temperature is overcome. However, Sol1260 sample exhibits a microstructure containing equiaxed grains. This means that by increasing the temperature to 1260 °C, the required driving force for recrystallization is provided.

A further investigation regarding material microstructure was done by calculating the kernel average misorientation (KAM). This value can be used to measure the local grain misorientation, which can be related to the dislocation density of the material [43]. More precisely, it represents the average misorientation between a defined point and its neighbors. In general, in deformed grains or when the strain energy is high within the grain, KAM is high as well. As recrystallized grains are strain-free, KAM can be used to study the fraction of recrystallized grains [44,45]. The KAM maps (Fig. 12) confirm that Sol1260 is a sample that has undergone a complete recrystallization process and, therefore, shows no internal strain.

High values of KAM imply orientation gradients in both as-built and Sol1230 conditions, which is relatively correlated to geometrically necessary dislocations (GND) [46].

3.3. Hardness evaluation

Hardness measurements were carried out for all conditions to better understand how different heat treatments and the resulting microstructure can affect the material's properties, and the results are given in Fig. 13.

Starting from the highest hardness value of 385 ± 5 in the as built condition, a softening takes place after the different heat treatments. The

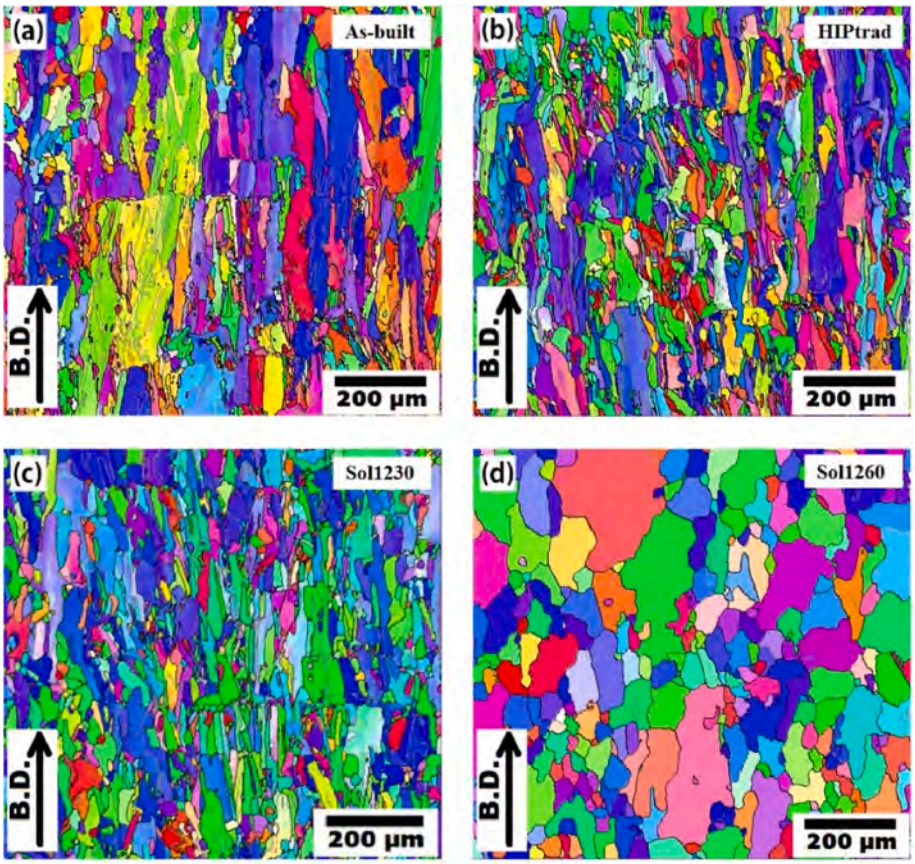

Fig. 11. – Crystal orientation maps obtained by EBSD from different samples: a) as-built, b) HIPtrad, c) Sol1230, and d) Sol1260.

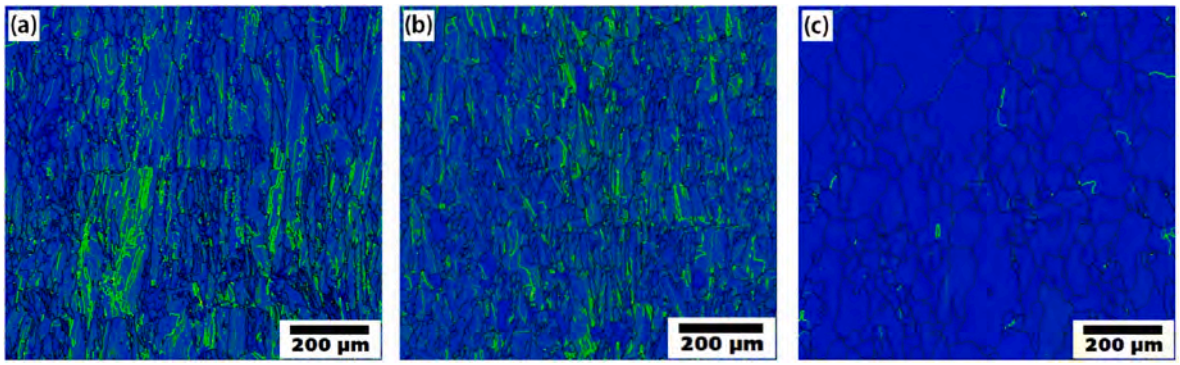

Fig. 12. – The kernel average misorientation (KAM) maps for a) as-built, b) Sol1230, and c) Sol1260 samples.

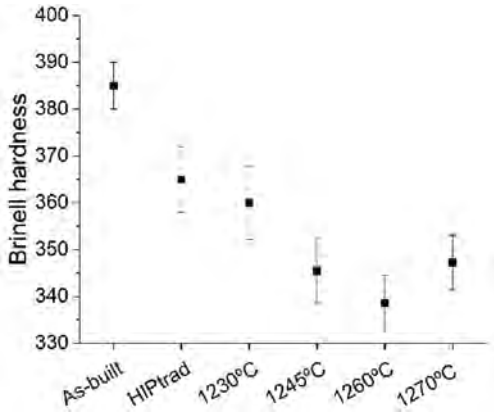

Fig. 13. – Brinell hardness values of the samples at different conditions.

as built hardness is markedly increased by the very fine microstructure and by the large level of strain accompanying it (see KAM maps above). HIP stage was already capable to release residual stresses and eliminate part of the unstable as built microstructural features. In the solution-annealed conditions, it is clear that the hardness decreases as the solubilizing temperature increases. For the Sol1230 sample, the hardness value is mainly attributed to the low grain size, which is about 15 μm. Increasing the temperature, grains tend to grow, and consequently, the hardness is reduced in accordance with the Hall-Petch equation. By changing the temperatures of solutioning, the volume fraction of γ′ remains almost constant, thus we can conclude that the effect of grain enlargement on the macro-hardness is indeed the most significant factor together with the progressive annihilation of the dislocation, which in turn decreases the residuals stresses in the material.

The HIPtrad and Sol1230 samples showed relatively the same hardness values. This fact can be related to the very close process temperature. By being solution annealed at two sub-solvus temperatures close to each other, they are expected to share almost similar hardness values.

Finally, the slight hardness increase observed in Sol1270 can be explained considering that, as the solution temperature gets higher, a progressively higher amount of primary γ′ is consumed at the grain boundaries and can precipitate again as secondary γ'. This effect, although very difficult to be measured with image analysis, is capable of generating ordered array of reinforcing particles within the grains. This condition will generate new possible interaction sites between the dislocations and γ' particles which results in the slightly higher hardness values observed. Since the movement and the interaction of the dislocations with the reinforcing particles is a process activated during the indentation itself, this condition cannot be identified with the KAM which remains low thanks to the strong recrystallization level achieved.

4. Conclusion

This study investigated the effect of different solution annealing temperatures on the microstructure of René 80 produced by PBF-LB technique. The recrystallization process was studied by observing the evolution of the size, of the shape, and of the fraction area of γ'. Performing the HIP at a sub-solvus temperature resulted in an unfavorable microstructure consisting of irregular-shaped γ′ precipitates and elongated grains along the thermal gradient. The grain size resulted in 45.5 ± 8.6 μm and 22 ± 0.7 μm in the XZ and XY planes, respectively, with a calculated aspect ratio of 2.0. This makes mandatory the application of a subsequent heat treatment and its optimization. To this purpose, it was observed that the grain size increased both in the XZ (from 15 μm to 59 μm) and XY (from 45 μm to 75 μm) planes by increasing the solution annealing temperature. Additionally, the hardness values tend to decrease by performing a post-processing treatment from 385 HB in as-built condition to 338.5 HB in the sample solution annealed at 1260 °C due to the grain coarsening. In particular, a significant reduction in the aspect ratio can be achieved raising the thermal setpoint at 1245 °C and at 1260 °C, where the calculated aspect ratio was reduced to 1.5 and 1.3, respectively. Regarding the γ′ phase, the results showed that the volume fraction and the size of γ′ phase did not change significantly by changing the solubilizing temperature from 1230 to 1260 °C. However, the change in its morphology was remarkable. It was seen that solubilization temperatures equal to or slightly higher than 1260 °C led to a uniform cuboidal structure of the strengthening phase. Moreover, by increasing the solutioning temperature, grains tended to be more equiaxed, confirming the activation of the recrystallization process. To assess the robustness of the process against thermal oscillations of industrial equipment (usually around ±10 °C), solution annealing at 1270 °C was also applied. This additional test suggested that even if an increase in the furnace temperature occurs, neither the morphology, size and volume fraction of the γ' nor the hardness change significantly, with no sign of detrimental effects like TIPs or incipient melting. In conclusion, optimizing post-processing heat treatment is critical for tailoring the microstructure of PBF-LB-produced René 80 superalloy. A solution annealing temperature around 1260 °C effectively achieves a desirable microstructure characterized by equiaxed grains and uniform cuboidal γ′ precipitates while maintaining acceptable mechanical properties.

Declaration of interests

The authors declare that they have no known competing financial interests or personal relationships that could have appeared to influence the work reported in this paper.

References

[1] Sidhu RK, Ojo OA, Chaturvedi MC. Sub-solidus melting of directionally solidified Rene 80 superalloy during solution heat treatment. J Mater Sci 2008;43:3612–7. https://doi.org/10.1007/s10853-008-2575-4.

[2] Tiley J, Viswanathan GB, Hwang JY, Shiveley A, Banerjee R. Evaluation of gamma prime volume fractions and lattice misfits in a nickel base superalloy using the external standard X-ray diffraction method. Mater Sci Eng, A 2010;528:32–6. https://doi.org/10.1016/j.msea.2010.07.036.

[3] Yang C, Xu Y, Nie H, Xiao X, Jia G, Shen Z. Effects of heat treatments on the microstructure and mechanical properties of Rene 80. Mater Des 2013;43:66–73. https://doi.org/10.1016/j.matdes.2012.06.039.

[4] Collier JP, Wong SH, Tien JK, Phillips JC, Tein JK. Effect of varying Al, Ti, and Nb content on the phase on the phase stability of Inconel 718. Metall Trans A 1988;19 A:1657–66. https://doi.org/10.1007/bf02645133.

[5] Barjesteh MM, Abbasi SM, Zangeneh Madar K, Shirvani K. The effect of heat treatment on characteristics of the gamma prime phase and hardness of the nickel-based superalloy Rene ® 80. Mater Chem Phys 2019;227:46–55. https://doi.org/10.1016/j.matchemphys.2019.01.038.

[6] Pyczak F, Neumeier S, Göken M. Influence of lattice misfit on the internal stress and strain states before and after creep investigated in nickel-base superalloys containing rhenium and ruthenium. Mater Sci Eng, A 2009;510–511:295–300. https://doi.org/10.1016/j.msea.2008.08.052.

[7] Rao SI, Parthasarathy TA, Dimiduk DM, Hazzledine PM. Discrete dislocation simulations of precipitation hardening in superalloys. Phil Mag 2004;84:3195–215. https://doi.org/10.1080/14786430412331284432.

[8] Aghaie-Khafri M, Farahany S. Creep life prediction of thermally exposed Rene 80 superalloy. J Mater Eng Perform 2010;19:1065–70. https://doi.org/10.1007/s11665-009-9584-6.

[9] Van Sluytman JS, Pollock TM. Optimal precipitate shapes in nickel-base γ-γ′ Alloys. Acta Mater 2012;60:1771–83. https://doi.org/10.1016/j.actamat.2011.12.008.

[10] Donachie MJ, Donachie SJ. Superalloys: a technical guide. https://doi.org/10.1016/B978-0-444-43022-9.50017-1; 2002.

[11] Nguyen L, Shi R, Wang Y, De Graef M. Acta Materialia Quantification of rafting of γ′ precipitates in Ni-based superalloys. Acta Mater 2016;103:322–33. https://doi.org/10.1016/j.actamat.2015.09.060.

[12] Baldan R, Rocha RLP, Tomasiello RB, Nunes CA, Costa AMS, Barboza MJR, Coelho GC, Rosenthal R. Solutioning and aging of MAR-M247 nickel-based superalloy. J Mater Eng Perform 2013;22:2574–9. https://doi.org/10.1007/s11665-013-0565-4.

[13] Atkinson HV, Davies S. Fundamental aspects of hot isostatic pressing: an overview. Metall Mater Trans A Phys Metall Mater Sci 2000;31:2981–3000. https://doi.org/10.1007/s11661-000-0078-2.

[14] Martelli PA, Sivo A, Calignano F, Bassini E, Biamino S, Ugues D. Parameters optimization and repeatability study on low-weldable nickel-based superalloy René 80 processed via laser powder–bed fusion (L-PBF). Metals 2023;13. https://doi.org/10.3390/met13020210.

[15] Marchese G, Bassini E, Calandri M, Ambrosio EP, Calignano F, Lorusso M, Manfredi D, Pavese M, Biamino S, Fino P. Microstructural investigation of as-fabricated and heat-treated Inconel 625 and Inconel 718 fabricated by direct metal laser sintering: contribution of Politecnico di Torino and Istituto Italiano di Tecnologia (IIT) di Torino. Met Powder Rep 2016;71:273–8. https://doi.org/10.1016/j.mprp.2016.06.002.

[16] Carter LN. Selective laser melting of nickel superalloys for high temperature applications, School of Metallurgy and Materials. 2013. p. 298.

[17] Shahsavari HA, Kokabi AH, Nategh S. Effect of preweld microstructure on HAZ liquation cracking of Rene 80 superalloy. Mater Sci Technol 2007;23:547–55. https://doi.org/10.1179/174328407X179539.

[18] Hilal H, Lancaster R, Jeffs S, Boswell J, Stapleton D, Baxter G. The influence of process parameters and build orientation on the creep behaviour of a laser powder bed fused ni-based superalloy for aerospace applications. Materials 2019;12. https://doi.org/10.3390/ma12091390.

[19] Bassini E, Sivo A, Martelli PA, Rajczak E, Marchese G, Calignano F, Biamino S, Ugues D. Effects of the solution and first aging treatment applied to as-built and post-HIP CM247 produced via laser powder bed fusion (LPBF). J Alloys Compd 2022;905:164213. https://doi.org/10.1016/j.jallcom.2022.164213.

[20] Newell DJ, O'Hara RP, Cobb GR, Palazotto AN, Kirka MM, Burggraf LW, Hess JA. Mitigation of scan strategy effects and material anisotropy through supersolvus annealing in LPBF IN718. Mater Sci Eng, A 2019;764:138230. https://doi.org/10.1016/j.msea.2019.138230.

[21] Xu J, Brodin H, Peng RL, Luzin V, Moverare J. Effect of heat treatment temperature on the microstructural evolution of CM247LC superalloy by laser powder bed fusion. Mater Charact 2022;185:111742. https://doi.org/10.1016/j.matchar.2022.111742.

[22] Zhou Y, Zhang Z, Zhao Z, Zhong Q. Effects of HIP temperature on the microstructural evolution and property restoration of a Ni-based superalloy. J Mater Eng Perform 2013;22:215–22. https://doi.org/10.1007/s11665-012-0246-8.

[23] Meid C, Dennstedt A, Ramsperger M, Pistor J, Ruttert B, Lopez-Galilea I, Theisen W, Körner C, Bartsch M. Effect of heat treatment on the high temperature fatigue life of single crystalline nickel base superalloy additively manufactured by means of selective electron beam melting. Scr Mater 2019;168:124–8. https://doi.org/10.1016/j.scriptamat.2019.05.002.

[24] Safari J, Nategh S. On the heat treatment of Rene-80 nickel-base superalloy. J Mater Process Technol 2006;176:240–50. https://doi.org/10.1016/j.jmatprotec.2006.03.165.

[25] Yang C, Xu Y, Nie H, Xiao X, Jia G, Shen Z. Effects of heat treatments on the microstructure and mechanical properties of Rene 80. Mater Des 2013;43:66–73. https://doi.org/10.1016/j.matdes.2012.06.039.

[26] Pan H, Zhu L, Cheng J, Xiao L, Ji H. Size-dependent microstructure evolution and formation mechanisms during the gas atomization process of FGH4113A Ni-based superalloy powder. Vacuum 2023;209:111751. https://doi.org/10.1016/J.VACUUM.2022.111751.

[27] Bassini E, Galech U, Soria T, Aristizabal M, Iturriza I, Biamino S, Ugues D. Effect of the particle size distribution on physical properties, composition, and quality of gas atomized Astroloy powders for HIP application. J Alloys Compd 2022;890:161631. https://doi.org/10.1016/J.JALLCOM.2021.161631.

[28] Martelli PA, Sivo A, Calignano F, Bassini E, Biamino S, Ugues D. Parameters optimization and repeatability study on low-weldable nickel-based superalloy René 80 processed via laser powder–bed fusion (L-PBF). Metals 2023;13. https://doi.org/10.3390/met13020210.

[29] ASTM E112-13. Standard test methods for determining average grain size. 2021. West Conshohocken, PA, USA.

[30] Marchese G, Aversa A, Bassini E. Microstructure and hardness evolution of solution annealed inconel 625/TiC composite processed by laser powder bed fusion. Metals 2021;11. https://doi.org/10.3390/met11060929.

[31] Sohrabpoor H, Salarvand V, Lupoi R, Chu Q, Li W, Aldwell B, Stanley W, O'Halloran S, Raghavendra R, Choi CH, Brabazon D. Microstructural and mechanical evaluation of post-processed SS 316L manufactured by laser-based powder bed fusion. J Mater Res Technol 2021;12:210–20. https://doi.org/10.1016/J.JMRT.2021.02.090.

[32] Van Sluytman JS, Moceri CJ, Pollock TM. A Pt-modified Ni-base superalloy with high temperature precipitate stability. Mater Sci Eng, A 2015;639:747–54. https://doi.org/10.1016/j.msea.2015.05.023.

[33] Xiang S, Mao S, Wei H, Liu Y, Zhang J, Shen Z, Long H, Zhang H, Wang X, Zhang Z, Han X. Selective evolution of secondary γ′ precipitation in a Ni-based single crystal superalloy both in the γ matrix and at the dislocation nodes. Acta Mater 2016;116:343–53. https://doi.org/10.1016/j.actamat.2016.06.055.

[34] Qiu CL, Andrews P. On the formation of irregular-shaped gamma prime and serrated grain boundaries in a nickel-based superalloy during continuous cooling. Mater Charact 2013;76:28–34. https://doi.org/10.1016/j.matchar.2012.11.012.

[35] Masoumi F, Shahriari D, Jahazi M, Cormier J, Devaux A. Kinetics and mechanisms of γ′ reprecipitation in a Ni-based superalloy. Sci Rep 2016;6:1–16. https://doi.org/10.1038/srep28650.

[36] Huang J, Ai C, Riu Y, Shang Y, Pei Y, Li S, Gong S, Zhang H. The effect of cooling rate from solution treatment on 0 reprecipitates and creep behaviors of a Ni-based superalloy single-crystal casting, vol. 12; 2022. https://doi.org/10.7449/1976/superalloys_1976_161_170.

[37] Martelli PA, Bassini E, Ugues D. The effect of hot isostatic pressing pressure level and solution annealing cooling rate on CM247 LC nickel-based superalloy processed by laser-based powder bed fusion. Progress in Additive Manufacturing 2024. https://doi.org/10.1007/s40964-024-00645-6.

[38] Johnson WC, Voorhees PW. Elastic interaction and stability of misfitting cuboidal inhomogeneities. J Appl Phys 1987;61:1610–9. https://doi.org/10.1063/1.338099.

[39] Doi M, Miyazaki T. The effect of elastic interaction energy on the shape of g' precipitate in Ni-based alloys. In: Superalloys; 1984. p. 7823–30.

[40] Rakoczy L, Milkovic O, Rutkowski B, Cygan R, Grudzien-Rakoczy M, Kromka F, Zielinska-Lipiec A. Characterization of γ' precipitates in cast Ni-Based superalloy and their behaviour at high-homologous temperatures studied by TEM and in situ XRD. Materials 2020;13. https://doi.org/10.3390/ma13102397.

[41] Bassini E, Marchese G, Cattano G, Lombardi M, Biamino S, Ugues D, Vallillo G, Picqué B. Influence of solutioning on microstructure and hardness of hot isostatically pressed Astroloy. J Alloys Compd 2017;723:1082–90. https://doi.org/10.1016/j.jallcom.2017.06.332.

[42] Mitchell RJ, Li HY, Huang ZW. On the formation of serrated grain boundaries and fan type structures in an advanced polycrystalline nickel-base superalloy. J Mater Process Technol 2009;209:1011–7. https://doi.org/10.1016/j.jmatprotec.2008.03.008.

[43] Saraf L. Kernel average misorientation confidence index correlation from FIB sliced Ni-Fe-Cr alloy surface. Microsc Microanal 2011;17:424–5. https://doi.org/10.1017/s1431927611002996.

[44] Harshavardhana N, Sivam SPSS, Kumar G, Saxena AK. A comparative study on misorientations to determine the extent of recrystallization in pure ETP copper. Phys Met Metallogr 2021;122:1279–87. https://doi.org/10.1134/S0031918X20140094.

[45] Harshavardhana N, Gururajan MP, Pant P. Microstructure engineering to optimize hardness and conductivity in electrolytic tough pitch copper. Metall Mater Trans A Phys Metall Mater Sci 2019;50:3566–77. https://doi.org/10.1007/s11661-019-05315-9.

[46] Rui SS, Niu LS, Shi HJ, Wei S, Tasan CC. Diffraction-based misorientation mapping: a continuum mechanics description. J Mech Phys Solids 2019;133. https://doi.org/10.1016/j.jmps.2019.103709.